





Functional properties of highly stable $\text{SrTi}_{0.95-x}\text{Zr}_{0.05}\text{Ni}_x\text{O}_{3-\delta}$ for use as oxygen transport membranes

Yuning Tang^{a,b,c,*} , Stefan Baumann^{a,c} , Arian Nijmeijer^b , Olivier Guillon^{a,c}, Wilhelm A. Meulenber^{a,b,c}

^a Forschungszentrum Jülich GmbH, Institute of Energy Materials and Devices (IMD-2), Jülich 52425, Germany

^b Inorganic Membranes, Faculty of Science and Technology, University of Twente, P.O. Box 217, Enschede 7500 AE, the Netherlands

^c Jülich Aachen Research Alliance: JARA-Energy, Jülich 52425, Germany

ARTICLE INFO

Keywords:

Oxygen transport membrane
Mixed ionic-electronic conductivity
Strontium titanate
STZN

ABSTRACT

Mixed ionic-electronic conducting ceramics have the potential to serve as oxygen transport membranes, thereby facilitating the separation of pure oxygen from air for a variety of chemical conversion applications. Given that the majority of the membrane reactors are operated in a reducing atmosphere, the stability of the materials is of great importance. In this study, the $\text{SrTi}_{0.95-x}\text{Zr}_{0.05}\text{Ni}_x\text{O}_{3-\delta}$ ($x = 0.01, 0.03, 0.05, 0.10, 0.15$) (STZN_x) powders were successfully synthesized and subsequently sintered into membranes. Ni substitution enhances oxygen permeability and catalytic activity via exsolution, while Zr improves structural stability by minimizing cation mismatch. XRD results indicate a Ni solubility limit below 15 %. An increase in the Ni content results in a corresponding enhancement in oxygen permeability, with STZN10 achieving the highest oxygen permeability while retaining a single phase. Thermochemical stability tests were conducted by annealing samples in a reducing atmosphere containing 2.9 % H₂ in Ar. The XRD and thermogravimetric analysis (TGA) demonstrate that STZN_x displays remarkable stability in reducing atmospheres. The presence of well-distributed Ni particles on the surface of STZN10 is observed after annealing in 2.9 % H₂/Ar at 900 °C for 48 h, proving the successful exsolution phenomenon aiming for improved catalytic activity for applications such as partial oxidation of methane. It can therefore be concluded that 10 % Ni-doped STZN10 is a promising material for oxygen transport membranes in catalytic membrane reactors.

1. Introduction

Oxygen is a very important gas that can be widely applied in different industrial areas. Despite the large availability of oxygen in the air, the process of separating it into a pure form requires a significant input of energy. The principal industrial techniques for the production of pure oxygen are cryogenic distillation and pressure swing adsorption (PSA), both of which require significant investment and operational expenses [1]. Ceramic materials that exhibit both ionic and electronic conductivity are well-regarded for their good performance in oxygen transport membranes (OTMs), which have been developed for a variety of energy applications, including air separation to produce pure oxygen for oxyfuel combustion [2] and medical purposes [3]. Additionally, the membranes can be utilized in membrane reactors for the production of commodity chemicals through a range of industrial reaction systems, including the water splitting [4,5], selective oxidation of ethane [6],

oxidative coupling of methane [7], and partial oxidation of methane [8, 9]. In the context of membrane reactor operating conditions, the gas environment typically contains CO, CO₂, H₂, or CH₄. Consequently, the membranes must exhibit high chemical stability under reducing environments. Strontium titanate (SrTiO₃), a highly stable perovskite material, typically exhibits dielectric properties. However, its electrical properties can be significantly altered through A/B-site doping. The potential for oxygen vacancies and electronic defects formation enables doped SrTiO₃ to conduct oxide ions, thus rendering it a mixed ionic-electronic conductor (MIEC) for use as OTM. Over the past decade, a variety of elements have been incorporated as dopants into the Sr or Ti sites of strontium titanate, such as Fe [10,11], Co [12,13], Al [14–16], Mg [17] and so on. However, the introduction of defects into the crystal lattice through doping can also result in the deterioration of stability. Cobalt-doped STO₃ can significantly enhance the oxygen permeability, but its stability remains a significant challenge [18]. Schulze-Küppers

* Corresponding author at: Forschungszentrum Jülich GmbH, Institute of Energy Materials and Devices (IMD-2), Jülich 52425, Germany.

E-mail address: y.tang@fz-juelich.de (Y. Tang).

<https://doi.org/10.1016/j.jeurceramsoc.2025.117715>

Received 11 April 2025; Received in revised form 23 July 2025; Accepted 24 July 2025

Available online 25 July 2025

0955-2219/© 2025 The Author(s). Published by Elsevier Ltd. This is an open access article under the CC BY license (<http://creativecommons.org/licenses/by/4.0/>).

et al. [10] investigated the functional properties of $\text{SrTi}_{1-x}\text{Fe}_x\text{O}_{3-\delta}$. The findings suggest that the Fe content of 25–35 % seems promising with considering the trade-off between stability and oxygen permeability. He et al. [17] identified a highly stable material $\text{SrMg}_{0.15}\text{Zr}_{0.05}\text{Ti}_{0.8}\text{O}_{3-\delta}$ (SMZ-Ti), which showed a good environment-induced oxygen permeation performance. The membrane can facilitate water splitting on one side while utilizing the permeated oxygen on the other side for methane reforming.

It is noteworthy that if the dopant element can exist in multiple oxidation states, the doped materials may also function as active catalytic centers [19]. Ni can adopt multiple oxidation states when incorporated into the titanium sublattice, like Ni^{2+} , Ni^{3+} and Ni^{4+} . This not only facilitates the modification of the material's electrical properties as a dopant but also renders it an active site for redox reactions on the surface of Ni-doped SrTiO_3 due to the associated valence change [20]. The phenomenon of Ni exsolution in reducing atmospheres has abundantly been reported in literature [21–25]. The synthesis and study of pure Ni-doped strontium titanate have been conducted by several researchers [20,26,27]. Nevertheless, the permeance as oxygen transport membrane materials has not yet been systematically characterized. For practical applications, especially under high-temperature or reducing environments, structural stability becomes a critical factor. In such conditions, the mismatch in ionic radii and valence states among B-site cations can lead to lattice distortions and phase instability. To mitigate this, Zr^{4+} is introduced as a co-dopant. With its high valence and excellent resistance to reduction, Zr^{4+} helps stabilize the cubic perovskite structure [17], thereby enhancing the material's suitability for demanding environments such as membrane reactors. Moreover, the ionic radius of Zr^{4+} is 0.72 Å, which is larger than that of Ti^{4+} (0.605 Å) and Ti^{3+} (0.67 Å). As a result, incorporating Zr into the perovskite structure can not only minimize cation mismatch and stabilize the cubic structure, but also increase the lattice parameters of STO. Therefore, we here study $\text{SrTi}_{0.95-x}\text{Zr}_{0.05}\text{Ni}_x\text{O}_{3-\delta}$ ($x = 0.01, 0.03, 0.05, 0.10, 0.15$) (STZN_x) aiming at high stability. The structure of the various materials has been characterized, and their permeability and electrical conductivity have been determined. Furthermore, the chemical stability and Ni exsolution phenomenon in reducing atmosphere (2.9 % H_2/Ar) were investigated.

2. Experimental

2.1. Powder preparation

Series of Ni-doped strontium titanates $\text{SrTi}_{0.95-x}\text{Zr}_{0.05}\text{Ni}_x\text{O}_{3-\delta}$ (STZN_x), with $x = 0.01, 0.03, 0.05, 0.10, 0.15$, were prepared by a solid-state reaction method. For convenience, $\text{SrTi}_{0.94}\text{Zr}_{0.05}\text{Ni}_{0.01}\text{O}_{3-\delta}$ is represented as STZN1 and so on in the following content. For the first step, SrCO_3 (Merck, 99 %), TiO_2 (Merck, 99 %), ZrO_2 (Merck, 99 %) and NiO (Merck, 99 %) powder were mixed with 3 mm Y-stabilized ZrO_2 milling balls and ethanol in a polyethylene bottle, and then homogenized on a roller bench for 48 h. The mass proportions of powder, ethanol, and balls were kept at a ratio of 1:2:3. The mixture was dried at 70 °C after milling and then sieved through 250 µm mesh. The calcination step was conducted at 1200 °C for 5 h. The powder obtained after calcination was ball milled, dried and sieved again with the same parameters as before. The bulk membranes were formed into discs using a PW10 uniaxial press (Ø 20 mm) (Fa. Paul Otto Weber GmbH, Remshalden), applying a pressure of 70 MPa for 1.5 min. 4 % wt. polyvinyl alcohol was added as binder to the mixture prior to pressing. The pressed STZN_x membranes were subsequently sintered at 1500 °C for 5 h, with heating and cooling rates of 5 K/min.

2.2. Characterization methods

The particle size distribution of all the powders was measured by a particle analyzer HORIBA LA-950V2 (Horiba European GmbH,

Germany). The crystal structures and phase compositions were analyzed based on X-ray diffraction (XRD) using a D4 ENDEAVOR diffractometer (Bruker, Germany) with $\text{Cu K}\alpha$ radiation. The diffraction angle (2θ) was scanned over a range of 10° to 80° with a step size of 0.02° and a dwell time of 0.75 s per step. Rietveld refinement analysis (Topas, Bruker, Germany) was carried out to determine the quantitative compositions and lattice parameters of the materials. The microstructure of the surface and cross section was observed via scanning electron microscopy (SEM) (Zeiss GeminiSEM 450) coupled with energy dispersive X-ray spectroscopy (EDS, Ultim Max 170, Oxford Instruments). A thin platinum layer was sputter-deposited onto the samples to improve their electronic conductivity before analysis. X-ray photoelectron spectroscopy (XPS) was performed using a PHI 5000 VersaProbe II system (ULVAC-PHI Inc., USA) equipped with a monochromatic $\text{Al K}\alpha$ X-ray source ($h\nu = 1486.6$ eV). The X-ray was operated at 50 W and 15 kV with a spot size of 200 µm. Survey spectra were acquired with a pass energy of 187.5 eV, a step size of 0.8 eV, and a dwell time of 100 ms/step. High-resolution spectra were recorded with a pass energy of 23.5 eV, a step size of 0.1 eV, and a dwell time of 100 ms/step. Charge correction was applied by referencing the main C 1 s peak to 285.0 eV. Cyclic thermogravimetric analysis (TGA) was performed using a STA449 F1 Jupiter calorimeter coupled with a QMS 403 C Aëolos (Netzsch) mass spectrometer under air and 2.9 % H_2/Ar atmospheres. The analysis was conducted up to a final temperature of 900 °C, with a heating and cooling rate of 10 K/min, and a gas flow rate of 50 mL/min. Each cycle included a holding time of 2 h for both the reduction and oxidation stages. The annealing experiments were carried out at 900 °C in reducing atmospheres (2.9 % H_2/Ar) for durations of 10 h and 48 h, respectively, with the heating and cooling rates of 5 °C/min. The surface changes of sintered pellets (Ø 8 mm×5 mm) were investigated before and after annealing. All fresh synthesized pellets were gas-tight, which has been confirmed by a He-leak rate detector (Quality test HTL 260, Pfeiffer Vacuum GmbH, Asslar, Germany).

2.3. Electrical conductivity

The total electrical conductivity (σ_t) was analyzed by electrochemical impedance spectroscopy (EIS) in air and Ar using an Alpha-A high performance frequency analyzer (Novocontrol Technologies, Germany). The measurements were conducted between 300 °C and 900 °C in a frequency range of 10^6 Hz to 10^{-1} Hz with three measurements per temperature step. Each temperature was maintained for 1 h before measurements to ensure equilibration of the oxygen vacancy concentration. The pellets (Ø8 mm×5 mm) were prepared by polishing the surfaces of a cylindrical specimen using 2500-grit sandpaper. Pt paste was brushed on both side of the pellets and sintered at 900 °C for 1 h to prepare Pt electrodes. The total conductivity σ_t of the sample was obtained according to Eq. (1):

$$\sigma_t = \frac{l}{R A} \quad (1)$$

Where R is the resistance (Ω) from the impedance spectroscopy, A is the electrode area (cm^2), and l is the sample thickness (cm).

The activation energy E_a was calculated according to Arrhenius Eq. (2):

$$\ln(\sigma_t \cdot T) = -\frac{E_a}{RT} + A \quad (2)$$

Where T is temperature (K), R is the ideal gas constant ($8.31446261815324 \text{ J}\cdot\text{K}^{-1}\cdot\text{mol}^{-1}$), A is a constant.

2.4. Oxygen permeation measurement

A 4-end mode set up was applied for the oxygen permeation experiments. The membranes were ground to approx. Ø 14.6 mm, polished to

1 mm thickness with 2500-grit sandpaper, and then sealed by two gold rings (\varnothing 13 mm) on the both sides in a vertical quartz glass housing. The measurements were conducted in air (250 mL min^{-1}) or pure O_2 (200 mL min^{-1}) at the feed side from $1000 \text{ }^\circ\text{C}$ to $800 \text{ }^\circ\text{C}$, respectively. Inert gas Ar was used as sweep gas at the permeate side with a flow rate of 50 mL min^{-1} when the feed gas was air or O_2 . The flow rate was controlled using mass flow controllers (MFCs, Bronkhorst, Germany). The concentration of O_2 and N_2 in the permeate gas was detected by a mass spectrometer (Omni Star, Pfeiffer Vacuum GmbH, Germany).

Oxygen transport is generally limited by either surface exchange reactions or bulk diffusion, depending on the membrane thickness (L). The key distinction between both limiting steps is the characteristic membrane thickness (L_c) [28–30]. If $L \gg L_c$, the transport is assumed to be only limited by bulk diffusion. According to literature studies, the characteristic thickness L_c for bulk-diffusion-limited oxygen transport in perovskite-type membranes is typically lower than $200 \text{ }\mu\text{m}$ [10,31,32]. Since our membranes are significantly thicker (1 mm), it is reasonable to assume that the oxygen flux is primarily governed by bulk diffusion. The oxygen flux in dense membranes is commonly described using a well-established model based on Wagner's theory in this case, which is typically expressed in the form of the standard Wagner equation [33,34] (Eq. (3)):

$$j(\text{O}_2) = \frac{R}{16F^2 \cdot L} \cdot T \cdot \sigma_{amb} \cdot \ln \frac{P'_{\text{O}_2}}{P''_{\text{O}_2}} \quad (3)$$

where R corresponds to the ideal gas constant, F is the Faraday constant, L is the thickness of the membrane, T is the membrane temperature, P'_{O_2} and P''_{O_2} are the oxygen partial pressure for oxygen rich and lean side of the membrane, respectively, and σ_{amb} is the ambipolar conductivity, given by Eq. (4):

$$\sigma_{amb} = \frac{\sigma_i \cdot \sigma_e}{\sigma_i + \sigma_e} \quad (4)$$

Where σ_i is the ionic conductivity and σ_e is the electronic conductivity. The ionic conductivity σ_i can be estimated with the respective ionic transference number t_i according to Eqs. (5–7).

$$\sigma_t = \sigma_i + \sigma_e \quad (5)$$

$$\frac{\sigma_{amb}}{\sigma_t} = t_i(1 - t_i) \quad (6)$$

$$\sigma_i = \sigma_t \cdot t_i \quad (7)$$

In the MIEC, if $\sigma_e \gg \sigma_i$, $\sigma_e \approx \sigma_t$, $\sigma_i \approx \sigma_{amb}$. The activation energy of σ_i was calculated as the same way as σ_i (Eq. (2)).

The driving force for OTMs is the gradient in oxygen partial pressure at the two sides of the membrane. Since the oxygen partial pressure depends on temperature, the driving force varies during the measurement. Therefore, the permeance can be determined by normalizing the oxygen permeation flux $j(\text{O}_2)$ with the oxygen partial pressure gradient ($\ln \frac{P'_{\text{O}_2}}{P''_{\text{O}_2}}$), and is defined as Eq. (8):

$$\text{Permeance} = \frac{j(\text{O}_2)}{\ln \frac{P'_{\text{O}_2}}{P''_{\text{O}_2}}} = \frac{R}{16F^2 \cdot L} \cdot T \cdot \sigma_{amb} \quad (8)$$

$$\ln(\text{permeance}) = -\frac{E_a}{RT} + A \quad (9)$$

The activation energy of permeance can be obtained by the Arrhenius approach (Eq. (9)), where R is the ideal gas constant and A is the pre-exponential factor.

Table 1

Particle size distribution of as-synthesized powders of STZN_x.

Name	Composition	d10 μm	d50 μm	d90 μm
STZN1	$\text{SrTi}_{0.94}\text{Zr}_{0.05}\text{Ni}_{0.01}\text{O}_{3.6}$	0.58	1.00	2.17
STZN3	$\text{SrTi}_{0.92}\text{Zr}_{0.05}\text{Ni}_{0.03}\text{O}_{3.6}$	0.58	0.99	2.18
STZN5	$\text{SrTi}_{0.90}\text{Zr}_{0.05}\text{Ni}_{0.05}\text{O}_{3.6}$	0.54	0.96	2.58
STZN10	$\text{SrTi}_{0.85}\text{Zr}_{0.05}\text{Ni}_{0.10}\text{O}_{3.6}$	0.55	1.02	3.09

3. Results and discussion

3.1. Crystal structure and microstructure

The d_{50} values of all the as-synthesized STZN_x powders are around $1 \text{ }\mu\text{m}$ (Table 1). The XRD patterns (Fig. 1) of all samples show a cubic perovskite structure (Pm3m), which was confirmed by Rietveld refinement. For the STZN15 sample, the XRD pattern shows a secondary phase with reflections corresponding to NiO, indicating that nickel is only partially dissolved into the perovskite structure during synthesis. This suggests that the solubility limit of Ni in perovskitic STZ is below 15%. Fig. 1(b) presents an enlarged view of the patterns from 30° to 35° . It is observed that the peaks of STZN_x shift towards higher angles as the Ni content increases, indicating a reduction in the lattice parameter. The cubic lattice parameters of STZN1, STZN3, STZN5, STZN10 and STZN15 are 3.918 , 3.917 , 3.916 , 3.914 and $3.913 \text{ }\text{\AA}$, respectively, according to the Rietveld refinement. The observed changes of the lattice parameter suggest that the introduced Ni most likely favors multiple oxidation states, like $+2$ ($0.69 \text{ }\text{\AA}$), $+3$ ($0.56 \text{ }\text{\AA}$) and $+4$ ($0.48 \text{ }\text{\AA}$) [20]. The presence of Ni^{4+} in a perovskite-like structure has already been confirmed by Takeda et al. in SrNiO_3 [35] and BaNiO_3 [36] compounds. Since STZN15 is not a single-phase material, it is excluded from the following discussion. XPS measurements were carried out to determine the valence of Ni on the membrane surface. As the Ni content of samples STZN1 and STZN3 is below the detection limit, only the results of STZN5 and STZN10 will be discussed (Fig. 2). The Ni $2p_{3/2}$ core-level spectra of samples STZN5 and STZN10 can be satisfactorily fitted using peak components characteristic of $\text{Ni}(\text{OH})_2$ [37], indicating that Ni primarily exists in the Ni^{2+} oxidation state on the membrane surface. However, the presence of Ni^{3+} cannot be entirely excluded, as it may exist in a relatively low concentration and therefore be difficult to detect. The existence of mixed-valence states of Ni in Ni-containing materials has been reported in previous studies, such as $\text{NiO/NiFe}_2\text{O}_4$ [38], $\text{Li}_{0.6}\text{NiO}_2$ [39], NiCo_2O_4 [40], $\text{Li}_2\text{NiTiO}_4$ [41] and Ni-doped $\text{Ba}_{1-x}\text{Sr}_x\text{TiO}_3$ [42]. The cross-sectional SEM images (Fig. 3) of the sintered pellets show that all the materials can achieve densification under the given sintering conditions, which is also confirmed by helium leakage experiments ($< 10^{-7} \text{ mbar}\cdot\text{L}\cdot\text{s}^{-1}$). It is worth noting that the grain size of STZN_x remains on the same scale. Ni has been reported as an effective sintering aid for perovskites [43–45]. The corresponding SEM images clearly indicate that the STZN10 membrane, with 10 % Ni doping, is significantly better sintered than the other STZN_x membranes with lower Ni content, further confirming the role of nickel dopant in enhancing membrane sintering.

3.2. Functional properties

3.2.1. Electrical conductivity

The electrical conductivity of STZN_x was calculated according to the EIS results. The conductivity increases with the Ni content increasing and the value in air ($p_{\text{O}_2}=0.2 \text{ atm}$) is higher than that in Ar ($\sim p_{\text{O}_2}=10^{-5} \text{ atm}$) (Fig. 4). It is reported that SrTiO_3 shows p-type conductivity at this oxygen partial pressure range [46]. In the p-type region, doped SrTiO_3 is a mixed conductor of oxygen vacancies and holes, however, with the hole conduction being dominant. Materials can generate more positive holes in air than in Ar due to the Eq. (10) [47]:

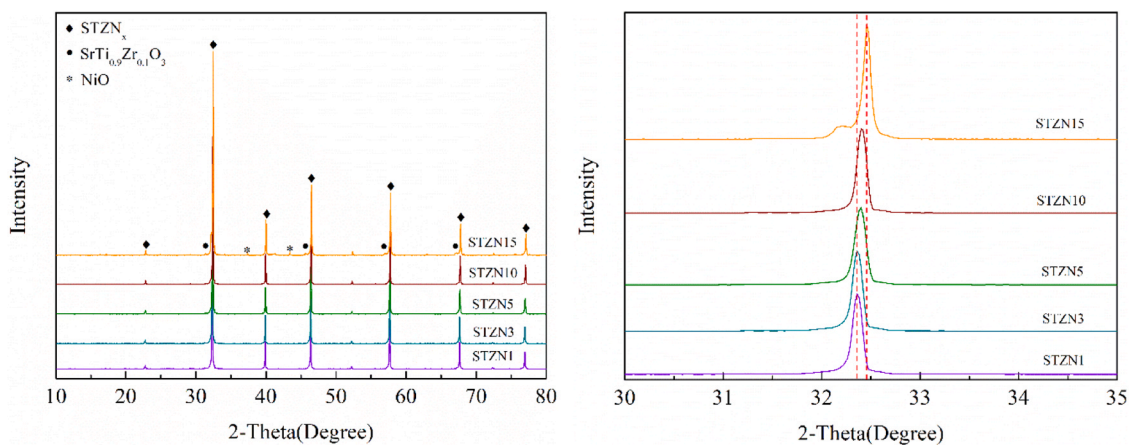


Fig. 1. XRD patterns of the as-synthesized membranes of STZN_x.

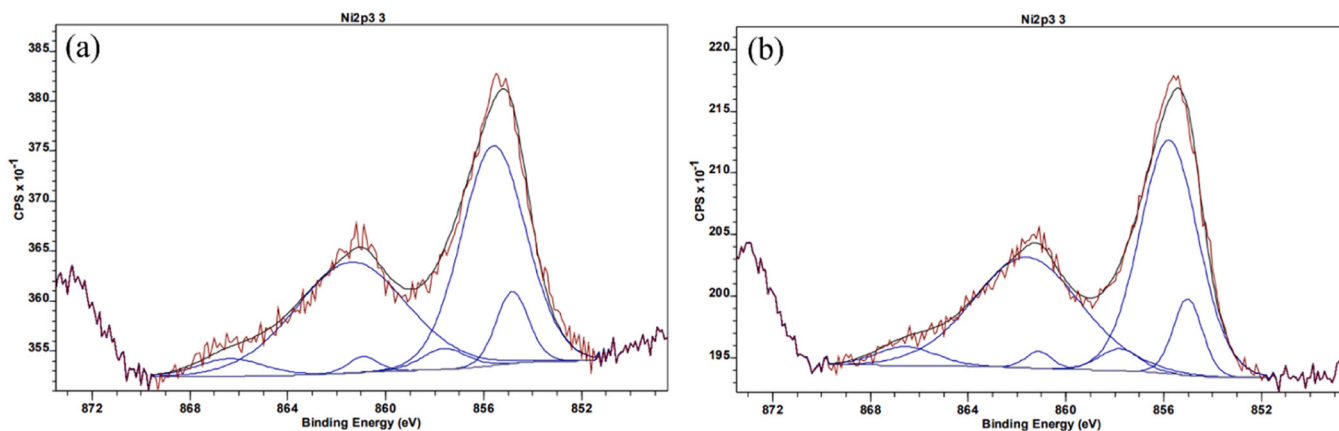


Fig. 2. XPS spectra of Ni 2p 3/2 of (a) STZN5 and (b) STZN10.

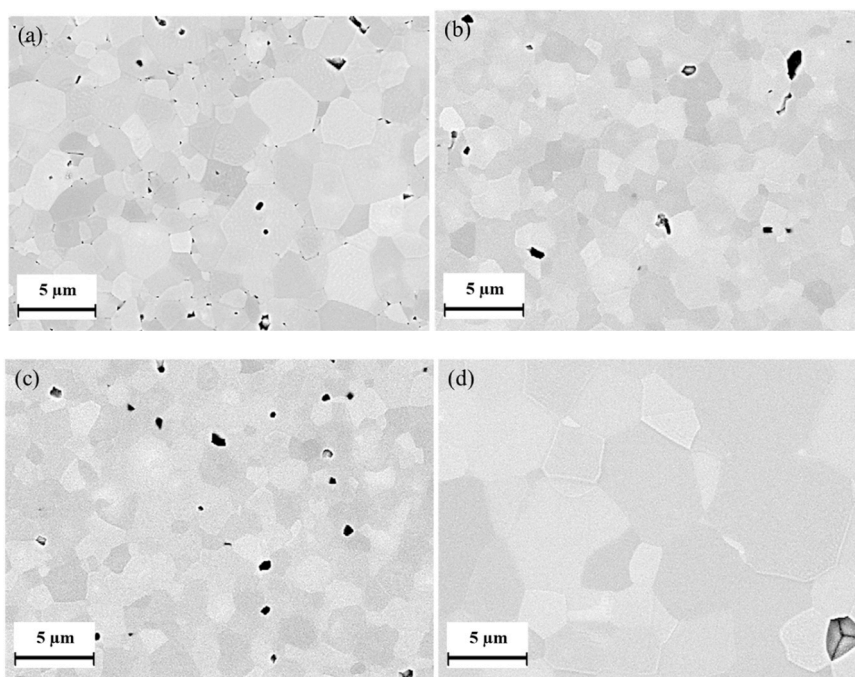


Fig. 3. Cross-section of the as-synthesized membranes of (a) STZN1, (b) STZN3, (c) STZN5 and (d) STZN10.

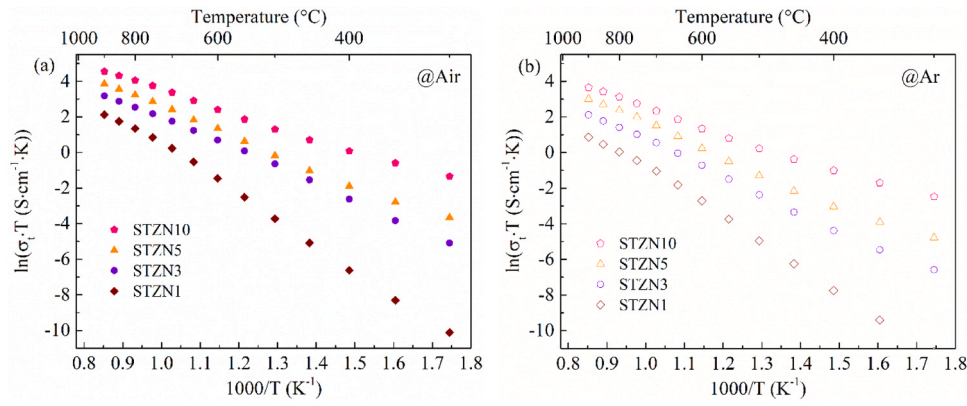


Fig. 4. The electrical conductivity of STZN_x in (a) air and (b) Ar.

Table 2

Electrical conductivity σ_t of STZN_x at 900 °C and activation energy E_a in air and Ar.

Name	σ_{t_Air} 900 °C (S/cm)	E_{a_Air} (600–900 °C) (kJ/mol)	σ_{t_Ar} 900 °C (S/cm)	E_{a_Ar} (600–900 °C) (kJ/mol)
STZN1	7.1×10^{-3}	101	2.0×10^{-3}	101
STZN3	2.1×10^{-2}	71	7.1×10^{-3}	80
STZN5	4.1×10^{-2}	72	1.7×10^{-2}	78
STZN10	8.1×10^{-2}	61	3.3×10^{-2}	66

$$\frac{1}{2}O_2 + V_o^\times = O_o^\times + 2h^\bullet \quad (10)$$

where V_o^\times , O_o^\times and h^\bullet represents an oxygen vacancy, an oxygen ion occupying an oxygen lattice site, and an electron hole, respectively. The superscripts \times and \bullet denote an electroneutral state and one positive effective charge, respectively. Table 2 lists the electrical conductivity of STZN_x at 900 °C and the activation energy in the application relevant temperature range 600–900 °C in air and Ar. The activation energy ranges from 61 kJ/mol to 101 kJ/mol in both atmospheres, with the value in Ar being higher than that in air.

3.2.2. Oxygen permeation

Oxygen permeation through ceramic membranes involves two primary processes [41]: gas-solid interfacial exchange occurring at the

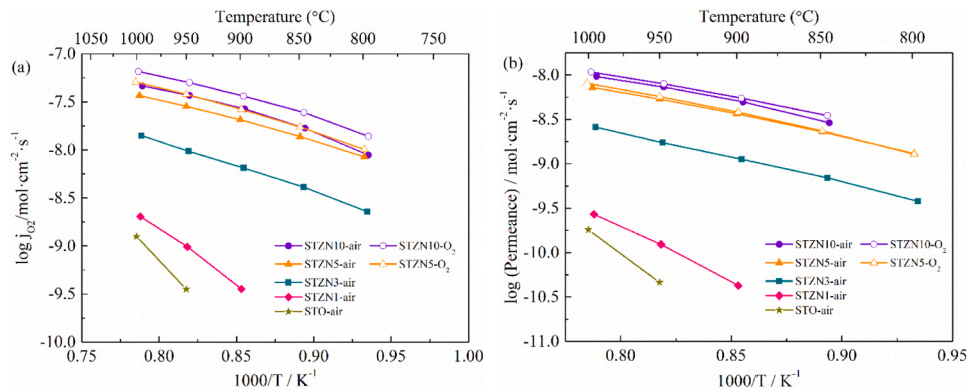


Fig. 5. (a) Permeation flux in air and O₂ and (b) Permeance of 1 mm thickness of STZN_x, respectively.

Table 3

Oxygen permeation flux, permeance and activation energy of STZN_x and doped-STO₃ materials at 1000 °C in air.

Composition	Oxygen flux mL·cm ⁻² ·min ⁻¹	Log (Permeance) mol·cm ⁻² ·s ⁻¹	E_a of Permeance (800–1000 °C) kJ·mol ⁻¹	Thickness (mm)	Ref.
SrTiO ₃ (STO)	1.85×10^{-3}	-9.74	353	1	[10]
SrTi _{0.75} Fe _{0.25} O _{3-δ} (STF25)	2.15×10^{-1}	-7.44	89	1	[10]
SrTi _{0.75} Co _{0.25} O _{3-δ} (STC25)	-	-7.45	79	1	[13]
SrTi _{0.65} Co _{0.35} O _{3-δ} (STC35)	-	-7.08	65	1	[13]
SrMg _{0.15} Zr _{0.05} Ti _{0.8} O _{3-δ} (SMZ-Ti)	2×10^{-2}	-	-	0.7	[17]
SrTi _{0.65} Fe _{0.35} O _{3-δ} (STF35)	2.46×10^{-1}	-7.27	82	1	[48]
SrTi _{0.6} Fe _{0.35} Ni _{0.05} O _{3-δ} (STFN005)	2.78×10^{-1}	-7.20	89	1	[48]
SrTi _{0.64} Zr _{0.05} Ni _{0.01} O _{3-δ} (STZN1)	2.72×10^{-3}	-9.57	236	1	This work
SrTi _{0.62} Zr _{0.05} Ni _{0.03} O _{3-δ} (STZN3)	1.89×10^{-2}	-8.58	108	1	This work
SrTi _{0.6} Zr _{0.05} Ni _{0.05} O _{3-δ} (STZN5)	4.09×10^{-2}	-8.22	98	1	This work
SrTi _{0.55} Zr _{0.05} Ni _{0.10} O _{3-δ} (STZN10)	6.23×10^{-2}	-8.02	103	1	This work

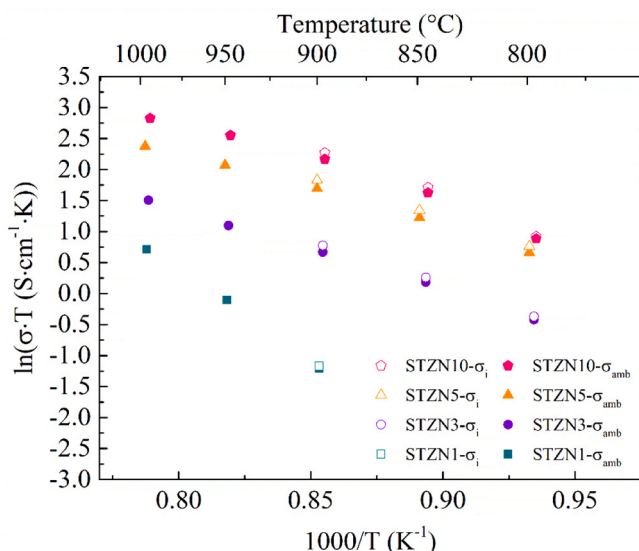


Fig. 6. Ambipolar conductivity σ_{amb} and ionic conductivity σ_i of STZN_x in air.

surface (surface exchange) and ion/electron transport within the bulk. For the 1 mm thick membranes, the oxygen permeation process is typically limited by bulk diffusion. Fig. 5(a) compares the oxygen permeation flux of STO and STZN_x measured under air/Ar (feed side/sweep side) and O₂/Ar conditions. The oxygen flux of STZN_x is higher than that of pure STO [10] and increases with increasing Ni content. Since the permeability of STZN1 and STZN3 is in a very low range, only STZN5 and STZN10 were tested in the O₂/Ar atmosphere for the following discussion. In addition, Fig. 5(a) indicates that the oxygen flux of STZN5 and STZN10 is higher in O₂/Ar compared to air/Ar due to the higher oxygen partial pressure gradient. The oxygen permeance, i.e. driving force-normalized oxygen permeation, is shown in Fig. 5(b). STZN5 and STZN10 can maintain similar values in two different conditions, confirming that the Wagner equation is applicable and, thus, bulk diffusion is the dominating transport mechanism. Table 3 compares the oxygen flux, permeance and activation energy E_a of STZN_x with other doped-STO₃ materials from literature at 1000 °C in air/Ar-gradients. The E_a values of STO (353 kJ mol⁻¹) and STZN1 (236 kJ mol⁻¹) are significantly higher than those of STZN3 (108 kJ mol⁻¹), STZN5 (98 kJ mol⁻¹), and STZN10 (103 kJ mol⁻¹). The significantly higher activation energy of the former samples is typically attributed to surface exchange limitations. Additionally, the oxygen permeation performance of STZN10 is found to be lower than that of other B-site doped STO₃ samples reported in the literature, such as Fe-doped STO₃ material SrTi_{1-x}Fe_xO_{3-δ} (STF_x) [10], cobalt-doped STO₃ material SrTi_{1-x}Co_xO_{3-δ} (STC_x) [13] and Fe/Ni co-doped STO₃ material SrTi_{0.65-x}Fe_{0.35}Ni_xO_{3-δ} (STFN_x) [48], with the exception of SrMg_{0.15}Zr_{0.05}Ti_{0.8}O_{3-δ} (SMZ-Ti) [17]. Although the oxygen permeation flux of STZN10 is lower than that of most B-site doped STO₃ materials, it can be improved through various strategies, such as the improvement of the oxygen partial pressure gradient across both sides of the membrane to a certain extent based on specific applications, the reduction of membrane thickness, the fabrication of asymmetric membranes, or the

Table 4

Ambipolar conductivity, ionic conductivity, activation energy and respective ionic transference numbers in air.

Name	σ_{amb_Air} 900 °C (S/cm)	σ_{i_Air} 900 °C (S/cm)	E_{a_amb} 800–1000 °C (kJ/mol)	E_{a_ionic} 800–900 °C (kJ/mol)	$t_{i_800\text{ °C}}$	$t_{i_900\text{ °C}}$
STZN1	2.54×10^{-4}	2.65×10^{-4}	-	-	-	3.75×10^{-2}
STZN3	1.67×10^{-3}	1.85×10^{-3}	108	119	5.44×10^{-2}	9.02×10^{-2}
STZN5	4.65×10^{-3}	5.32×10^{-3}	98	111	8.42×10^{-2}	1.31×10^{-1}
STZN10	7.48×10^{-3}	8.30×10^{-3}	110	141	4.37×10^{-2}	1.03×10^{-1}

addition of a catalytic layer to the material's surface.

Fig. 6 shows the ambipolar conductivity and ionic conductivity of STZN_x in air. The graph shows that both conductivities are of the same order of magnitude and increase with increasing Ni content. The ionic conductivity is slightly higher than that of ambipolar conductivity, indicating the electronic conductivity is much higher than the ionic conductivity. Table 4 lists the ambipolar conductivity, ionic conductivity and the corresponding activation energy as well as the respective ionic transference numbers in air. It can be noted that the activation energy of the ambipolar conductivity is lower than the activation energy of the ionic conductivity. Since the ambipolar conductivity is determined by both the ionic conductivity and electronic conductivity of the material, this reduction reflects a significant contribution of electron transport, which lowers the overall activation energy. In addition, the ionic conductivity of the materials is more sensitive to temperature due to its higher activation energy compared to electronic and ambipolar conductivity.

3.3. Thermo-chemical stability

TG measurements and annealing measurements are designed to evaluate the thermo-chemical stability of the materials.

Fig. 7 illustrates the mass change over time for different STZN_x samples upon cyclic exposure to air and 2.9 % H₂/Ar atmosphere. The

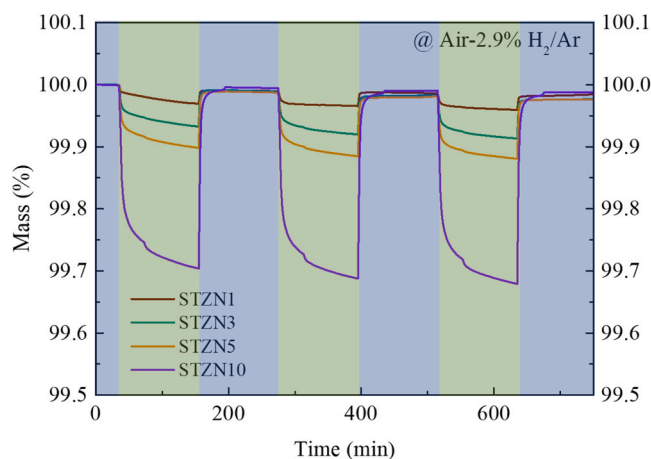


Fig. 7. Three-cycle TG measurements of STZN_x in air (marked in blue) and 2.9 % H₂/Ar atmospheres (marked in green).

Table 5

Mass loss of STZN_x at different stages.

Composition	First cycle mass loss H ₂ / Ar	Second cycle mass loss H ₂ / Ar	Third cycle mass loss H ₂ / Ar	Final mass loss _{air}
STZN1	0.030 %	0.035 %	0.041 %	0.017 %
STZN3	0.067 %	0.081 %	0.087 %	0.024 %
STZN5	0.102 %	0.115 %	0.120 %	0.024 %
STZN10	0.296 %	0.313 %	0.321 %	0.013 %

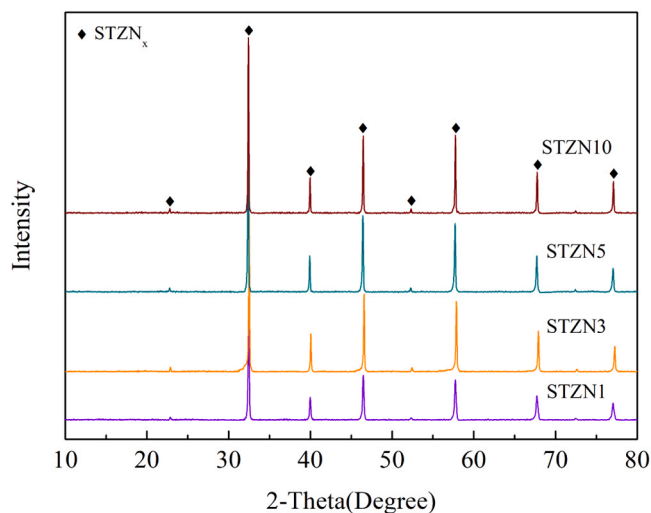


Fig. 8. XRD patterns of STZN_x after three-cycle TG measurement.

mass of all samples is observed to decrease during the periods in the reducing 2.9 % H₂/Ar environment (indicated in green) due to oxygen release during reduction of B-site elements, and subsequently recovers due to re-oxidation during the air exposure periods (indicated in blue). The mass loss of STZN_x under the reducing condition increases with increasing Ni content. Notably, a two-step mass loss is observed in the STZN10 curve, which can be estimated to the sequential reduction of the same element, such as Ni⁴⁺ → Ni³⁺ → Ni²⁺ → Ni, or the stepwise reduction of the different B-site elements, such as Ni and Ti. Table 5 compares the mass loss of STZN_x at different stages. This indicates that the mass loss slightly increases with the number of cycles. But all the values are less than 0.33 %, which is very small. The mass change of all the materials is practically fully reversible confirmed by XRD patterns showing single phase structure after the final reoxidation step of TG measurements (Fig. 8). Considering the highly reducing conditions of 2.9 % H₂/Ar at 900 °C STZN_x materials show excellent cyclic reduction stability. Therefore, STZN10 is identified as a promising candidate for OTMs in membrane reactors, given its excellent stability and the highest oxygen permeability among the STZN_x series materials.

Sintered STZN_x pellets were annealed in a 2.9 % H₂/Ar atmosphere at 900 °C for either 10 h or 48 h to evaluate their stability under highly reducing conditions. The XRD patterns (Fig. 9) indicate that all materials still maintain a single-phase structure after annealing demonstrating excellent stability. The surfaces of as-synthesized and annealed STZN10 were characterized using SEM coupled with EDS analysis (Fig. 10(a-d)). The surface of the sample annealed for 10 h displays a similar morphology to that of the as-synthesized pellets, with no detectable Ni on the surface. However, as the annealing time increases, Ni exsolution

becomes obvious on the surface of the sample annealed for 48 h (Fig. 10(c)), with the exsolved Ni highlighted in yellow in the EDS mapping (Fig. 10(d)). The prominently bright yellow region in Fig. 10(d) is attributed to the reduction of a remaining NiO particle, which was not dissolved during powder synthesis. The cross-sectional SEM image (Fig. 10(e)) reveals a uniform microstructure without detectable Ni segregation in the bulk of the STZN10 sample after 48 h of annealing.

4. Conclusions

This study systematically investigates the microstructures, functional properties and stability of STZN_x series materials for use as OTMs. The single-phase materials STZN1, STZN3, STZN5 and STZN10 were successfully prepared with the solid-state reaction method. XRD characterization shows that the solubility limit of Ni in the perovskite is below 15 % in this case. The findings demonstrate that the substitution of Ti with Ni can considerably improve the oxygen permeability and conductivity of STZN_x in comparison to that of pure STO. It can be observed that an increase in Ni content results in enhanced performance. All samples still are single phase materials even annealed in 2.9 % H₂/Ar for 48 h. The surface of STZN10 exhibits uniformly distributed Ni particles after annealing, which can be regarded as active catalytic centers for chemical reactions in a membrane reactor. Three-cycle TG measurements illustrate that all the STZN_x materials exhibit reversible oxygen exchange and, thus, excellent stability in a reducing atmosphere.

Although the oxygen permeation flux of STZN10 is lower than that of most B-site doped STO₃ materials, it demonstrates unique potential for applications as oxygen transport membranes (OTMs) in membrane reactors, particularly in processes involving hydrocarbons at high temperatures. The advantages of STZN10 lie in two key aspects: (1) the incorporation of Ni creates catalytically active sites on the material surface due to the Ni exsolution phenomenon in reducing atmosphere; and (2) exceptional structural stability under harsh conditions. To enhance its oxygen permeability, several optimization strategies can be implemented, such as establishing a gradient oxygen partial pressure driving force to a certain extent based on specific applications, fabricating submicron-scale ultrathin dense layers (e.g., thickness <50 μm), designing asymmetric membranes with a support layer-functional dense layer composite structure, or the addition of a catalytic layer to the material's surface to reduce surface exchange resistance. These approaches make STZN10 a promising candidate for high temperature membrane reactors involving separation and reaction processes like partial oxidation of methane, combining catalytic activity with high stability.

CRedit authorship contribution statement

Olivier Guillon: Writing – review & editing, Resources. **Arian Nijmeijer:** Writing – review & editing, Supervision. **Stefan Baumann:**

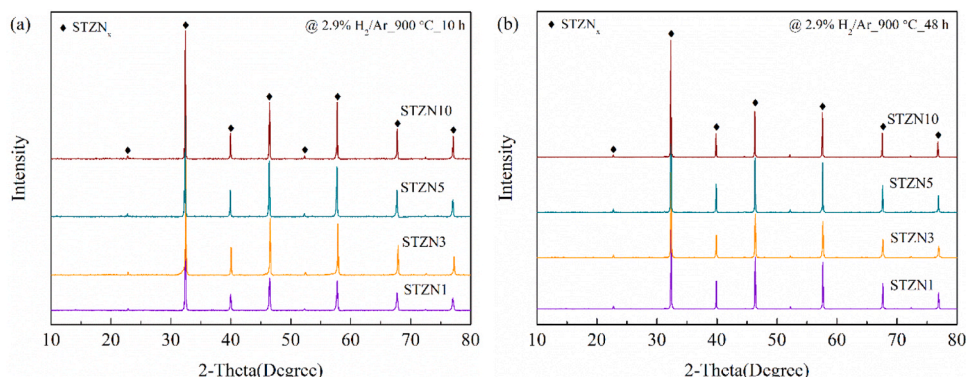


Fig. 9. XRD patterns of STZN_x annealed in 2.9 % H₂/Ar at 900 °C for (a) 10 h and (b) 48 h.

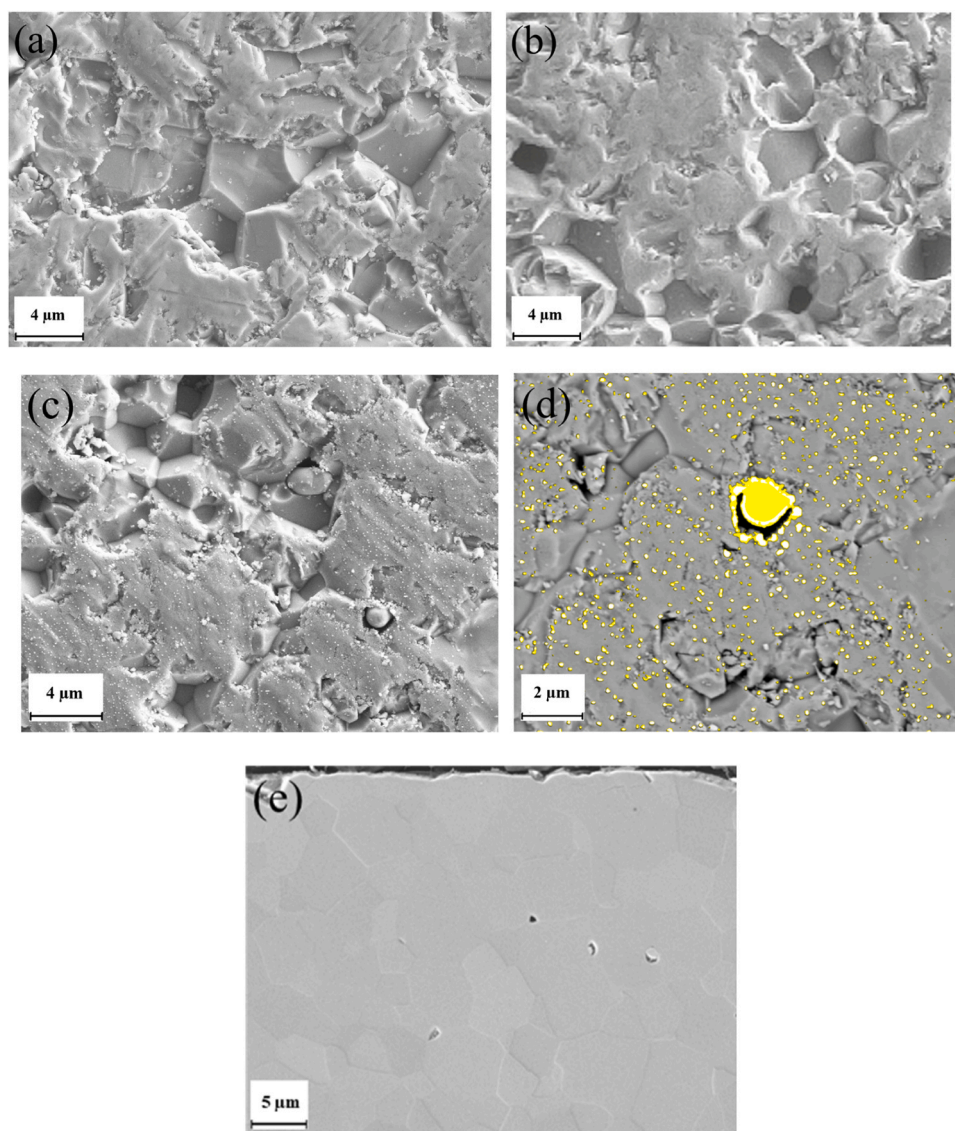


Fig. 10. Surface and cross-sectional SEM images of STZN10 in different states: (a) as-synthesized, (b) annealed for 10 h, (c) annealed for 48 h along with (d) EDS mapping; and (e) cross-section after 48 h of annealing.

Writing – review & editing, Supervision, Resources, Project administration, Data curation, Conceptualization. **Meulenberg Wilhelm Albert:** Writing – review & editing, Supervision, Resources, Project administration. **Yuning Tang:** Writing – review & editing, Writing – original draft, Visualization, Validation, Methodology, Investigation, Funding acquisition, Formal analysis, Data curation, Conceptualization.

Declaration of Competing Interest

The authors declare that they have no known competing financial interests or personal relationships that could have appeared to influence the work reported in this paper.

Acknowledgements

Yuning Tang gratefully acknowledges the China Scholarship Council for financial support under No 202006150006. The authors gratefully acknowledge Dr. Doris Sebold for SEM measurements, Dr. Yoo Jung Sohn for XRD measurements and Rietveld refinements, Dr. Heinrich Hartmann for XPS analysis, Ms Marie Theres Gerhards for TG measurements, Mr. Volker Bader and Mr. Stefan Heinz for experimental

support and sample preparation.

References

- [1] R.W. Baker, Future directions of membrane gas separation technology, *Ind. Eng. Chem. Res.* 41 (6) (2002) 1393–1411.
- [2] R. Kiebach, S. Pirou, L. Martinez Aguilera, A.B. Haugen, A. Kaiser, P.V. Hendriksen, M. Balaguer, J. Garcia-Fayos, J.M. Serra, F. Schulze-Küppers, M. Christie, L. Fischer, W.A. Meulenberg, S. Baumann, A review on dual-phase oxygen transport membranes: from fundamentals to commercial deployment, *J. Mater. Chem. A* 10 (5) (2022) 2152–2195.
- [3] F. Sjöberg, M. Singer, The medical use of oxygen: a time for critical reappraisal, *J. Intern. Med.* 274 (6) (2013) 505–528.
- [4] H. Jiang, H. Wang, S. Werth, T. Schiestel, J. Caro, Simultaneous production of hydrogen and synthesis gas by combining water splitting with partial oxidation of methane in a hollow-fiber membrane reactor, *Angew. Chem.* 47 (48) (2008) 9341–9344.
- [5] G. He, Y. Ling, H. Jiang, A. Toghian, Barium titanate as a highly stable oxygen permeable membrane reactor for hydrogen production from thermal water splitting, *ACS Sustain. Chem. Eng.* 9 (33) (2021) 11147–11154.
- [6] F.T. Akin, Y.S. Lin, Selective oxidation of ethane to ethylene in a dense tubular membrane reactor, *J. Membr. Sci.* 209 (2) (2002) 457–467.
- [7] H.R. Godini, S. Xiao, M. Kim, N. Holst, S. Jašo, O. Görke, J. Steinbach, G. Wozny, Experimental and model-based analysis of membrane reactor performance for methane oxidative coupling: effect of radial heat and mass transfer, *J. Ind. Eng. Chem.* 20 (2014) 1993–2002.

- [8] A.H. Elbadawi, L. Ge, Z. Li, S. Liu, S. Wang, Z. Zhu, Catalytic partial oxidation of methane to syngas: review of perovskite catalysts and membrane reactors, *Catal. Rev.* 63 (1) (2021) 1–67.
- [9] W. Bai, J. Feng, C. Luo, P. Zhang, H. Wang, Y. Yang, Y. Zhao, H. Fan, A comprehensive review on oxygen transport membranes: development history, current status, and future directions, *Int. J. Hydrog. Energy* 46 (73) (2021) 36257–36290.
- [10] F. Schulze-Küppers, S.F.P. ten Donkelaar, S. Baumann, P. Prigorodov, Y.J. Sohn, H. J.M. Bouwmeester, W.A. Meulenber, O. Guillon, Structural and functional properties of $\text{SrTi}_{1-x}\text{Fe}_x\text{O}_{3-\delta}$ ($0 < x < 1$) for the use as oxygen transport membrane, *Sep. Purif. Technol.* 147 (2015) 414–421.
- [11] V. Metlenko, W. Jung, S.R. Bishop, H.L. Tuller, R.A. De Souza, Oxygen diffusion and surface exchange in the mixed conducting oxides $\text{SrTi}_{(1-y)}\text{Fe}_y\text{O}_{(3-\delta)}$, *Physical chemistry chemical physics*, PCCP 18 (42) (2016) 29495–29505.
- [12] X. Li, H. Zhao, N. Xu, X. Zhou, C. Zhang, N. Chen, Electrical conduction behavior of La, Co co-doped SrTiO_3 perovskite as anode material for solid oxide fuel cells, *Int. J. Hydrog. Energy* 34 (15) (2009) 6407–6414.
- [13] Y. Liu, S. Baumann, F. Schulze-Küppers, D.N. Mueller, O. Guillon, Co and Fe co-doping influence on functional properties of SrTiO_3 for use as oxygen transport membranes, *J. Eur. Ceram. Soc.* 38 (15) (2018) 5058–5066.
- [14] L.A. Donyushkina, V.A. Gorbunov, A.A. Babkina, N.O. Esina, High-temperature electrical transport in Al-doped calcium and strontium titanates, *Ionics* 9 (1) (2003) 67–70.
- [15] Z. Zhao, R.V. Goncalves, S.K. Barman, E.J. Willard, E. Byle, R. Perry, Z. Wu, M. N. Huda, A.J. Moulé, F.E. Osterloh, Electronic structure basis for enhanced overall water splitting photocatalysis with aluminum doped SrTiO_3 in natural sunlight, *Energy Environ. Sci.* 12 (4) (2019) 1385–1395.
- [16] M.A.K.Y. Shah, Y. Lu, N. Mushtaq, M. Yousaf, S. Rauf, M.I. Asghar, P.D. Lund, B. Zhu, Perovskite Al-SrTiO₃ semiconductor electrolyte with superionic conduction in ceramic fuel cells, *Sustain. Energy Fuels* 6 (16) (2022) 3794–3805.
- [17] G. He, W. Liang, C.L. Tsai, X. Xia, S. Baumann, H. Jiang, W.A. Meulenber, Chemical environment-induced mixed conductivity of titanate as a highly stable oxygen transport membrane, *iScience* 19 (2019) 955–964.
- [18] Y. Liu, V. Motalov, S. Baumann, D. Sergeev, M. Müller, Y.J. Sohn, O. Guillon, Thermochemical stability of Fe- and co-functionalized perovskite-type SrTiO_3 oxygen transport membrane materials in syngas conditions, *J. Eur. Ceram. Soc.* 39 (15) (2019) 4874–4881.
- [19] K. Kendall, M. Kendall, High-temperature solid oxide fuel cells for the 21st century: fundamentals, design and applications, Elsevier, 2015.
- [20] A. Mizera, E. Drożdż, Studies on structural, redox and electrical properties of Ni-doped strontium titanate materials, *Ceram. Int.* 46 (15) (2020) 24635–24641.
- [21] M.L. Weber, M. Wilhelm, L. Jin, U. Breuer, R. Dittmann, R. Waser, O. Guillon, C. Lenser, F. Gunkel, Exsolution of embedded nanoparticles in defect engineered perovskite layers, *ACS Nano* 15 (3) (2021) 4546–4560.
- [22] T. Zhu, H.E. Troiani, L.V. Mogni, M. Han, S.A. Barnett, Ni-substituted $\text{Sr}(\text{Ti},\text{Fe})\text{O}_3$ SOFC anodes: achieving high performance via metal alloy nanoparticle exsolution, *Joule* 2 (3) (2018) 478–496.
- [23] D. Papargyriou, D.N. Miller, J.T. Sirt Irvine, Exsolution of Fe–Ni alloy nanoparticles from $(\text{La},\text{Sr})(\text{Cr},\text{Fe},\text{Ni})\text{O}_3$ perovskites as potential oxygen transport membrane catalysts for methane reforming, *J. Mater. Chem. A* 7 (26) (2019) 15812–15822.
- [24] J. Wang, D. Kalaev, J. Yang, I. Waluyo, A. Hunt, J.T. Sadowski, H.L. Tuller, B. Yildiz, Fast surface oxygen release kinetics accelerate nanoparticle exsolution in perovskite oxides, *J. Am. Chem. Soc.* 145 (3) (2023) 1714–1727.
- [25] W. O’Leary, L. Giordano, J. Park, S.S. Nonnenmann, Y. Shao-Horn, J.L.M. Rupp, Influence of Sr-Site deficiency, Ca/Ba/La doping on the exsolution of Ni from SrTiO_3 , *J. Am. Chem. Soc.* 145 (25) (2023) 13768–13779.
- [26] K.A. Müller, W. Berlinger, R.S. Rubins, Observation of two charged states of a nickel-oxygen vacancy pair in SrTiO_3 by paramagnetic resonance, *Phys. Rev.* 186 (2) (1969) 361–371.
- [27] A.M. Beale, M. Paul, G. Sankar, R.J. Oldman, C.R.A. Catlow, S. French, M. Fowles, Combined experimental and computational modelling studies of the solubility of nickel in strontium titanate, *J. Mater. Chem.* 19 (25) (2009) 4391.
- [28] F. Mauvy, J.M. Bassat, E. Boehm, P. Dordor, J.C. Grenier, J.P. Loup, Chemical oxygen diffusion coefficient measurement by conductivity relaxation—correlation between tracer diffusion coefficient and chemical diffusion coefficient, *J. Eur. Ceram. Soc.* 24 (6) (2004) 1265–1269.
- [29] P.-M. Geoffroy, E. Blond, N. Richet, T. Chartier, Understanding and identifying the oxygen transport mechanisms through a mixed-conductor membrane, *Chem. Eng. Sci.* 162 (2017).
- [30] R. Cox-Galhotra, S. McIntosh, Unreliability of simultaneously determining kchem and Dchem via conductivity relaxation for surface-modified $\text{La}_{0.6}\text{Sr}_{0.4}\text{Co}_{0.2}\text{Fe}_{0.8}\text{O}_{3-\delta}$, *Solid State Ion.* 181 (2010) 1429–1436.
- [31] H.J.M. Bouwmeester, H. Kruidhof, A.J. Burggraaf, Importance of the surface exchange kinetics as rate limiting step in oxygen permeation through mixed-conducting oxides, *Solid State Ion.* 72 (1994) 185–194.
- [32] J.E. ten Elshof, H.J.M. Bouwmeester, H. Verweij, Oxygen transport through $\text{La}_{1-x}\text{Sr}_x\text{FeO}_{3-\delta}$. I. Permeation in air/He gradients, *Solid State Ion.* 81 (1996).
- [33] J. Sunarso, S. Baumann, J.M. Serra, W.A. Meulenber, S. Liu, Y.S. Lin, J.C. Diniz da Costa, Mixed ionic–electronic conducting (MIEC) ceramic-based membranes for oxygen separation, *J. Membr. Sci.* 320 (1–2) (2008) 13–41.
- [34] A. Arratibel Plazaola, A. Cruellas Labella, Y. Liu, N. Badiola Porras, D.A. Pacheco Tanaka, M.V. Sint Annaland, F. Gallucci, Mixed ionic-electronic conducting membranes (MIEC) for their application in membrane reactors: a review, *Processes* 7 (3) (2019) 128.
- [35] Y. Takeda, T. Hashino, H. Miyamoto, F. Kanamaru, S. Kume, M. Koizumi, Synthesis of SrNiO_3 and related compound, $\text{Sr}_2\text{Ni}_2\text{O}_5$, *J. Inorg. Nucl. Chem.* 34 (5) (1972) 1599–1601.
- [36] Y. Takeda, F. Kanamura, M. Shimada, M. Koizumi, The crystal structure of BaNiO_3 , *Acta Crystallogr. Sect. B* 32 (8) (1976) 2464–2466.
- [37] M.C. Biesinger, B.P. Payne, L.W.M. Lau, A. Gerson, R.S.C. Smart, X-ray photoelectron spectroscopic chemical state quantification of mixed nickel metal, oxide and hydroxide systems, *Surf. Interface Anal.* 41 (4) (2009) 324–332.
- [38] G. Liu, X. Gao, K. Wang, D. He, J. Li, Uniformly mesoporous $\text{NiO}/\text{NiFe}_2\text{O}_4$ biphasic nanorods as efficient oxygen evolving catalyst for water splitting, *Int. J. Hydrog. Energy* 41 (40) (2016) 17976–17986.
- [39] X. Xiao, Y. Xu, Soft chemical synthesis and characterization of lithium nickel oxide electrode materials, *J. Mater. Sci.* 31 (24) (1996) 6449–6454.
- [40] J.F. Marco, J.R. Gancedo, M. Gracia, J.L. Gautier, E.I. Ríos, H.M. Palmer, C. Greaves, F.J. Berry, Cation distribution and magnetic structure of the ferrimagnetic spinel NiCo_2O_4 , *J. Mater. Chem.* 11 (12) (2001) 3087–3093.
- [41] Y. Wang, Y. Wang, F. Wang, Facile molten salt synthesis of $\text{Li}_2\text{NiTiO}_4$ cathode material for Li-ion batteries, *Nanoscale Res. Lett.* 9 (1) (2014) 197.
- [42] A.I. Lebedev, I.A. Sluchinskaya, On the nature of change in Ni oxidation state in BaTiO_3 - SrTiO_3 system, *Ferroelectrics* 501 (1) (2016) 1–8.
- [43] M.T. Colomer, J.A. Kilner, Effect of sintering time on structural, microstructural and chemical composition of Ni-doped lanthanum gallate perovskites, *J. Solid State Chem.* 228 (2015) 167–173.
- [44] C. Duan, J. Huang, N. Sullivan, R. O’Hayre, Proton-conducting oxides for energy conversion and storage, *Appl. Phys. Rev.* 7 (1) (2020).
- [45] M. Yang, F. He, C. Zhou, F. Dong, G. Yang, W. Zhou, Z. Shao, New perovskite membrane with improved sintering and self-reconstructed surface for efficient hydrogen permeation, *J. Membr. Sci.* 620 (2021) 118980.
- [46] C. Ohly, S. Hoffmann-Eifert, X. Guo, J. Schubert, R. Waser, Electrical conductivity of epitaxial SrTiO_3 thin films as a function of oxygen partial pressure and temperature, *J. Am. Ceram. Soc.* 89 (9) (2006) 2845–2852.
- [47] X. Zhu, W. Yang, Introduction to Mixed Ionic–Electronic Conducting Membranes, in: X. Zhu, W. Yang (Eds.), *Mixed Conducting Ceramic Membranes: Fundamentals, Materials and Applications*, Springer Berlin Heidelberg, Berlin, Heidelberg, 2017, pp. 1–10.
- [48] Y. Tang, S. Baumann, M. Müller, D. Sebald, A. Nijmeijer, O. Guillon, W. A. Meulenber, Ni-doping influence on functional properties of $\text{SrTi}_{0.65}\text{Fe}_{0.35}\text{O}_{3-\delta}$ for use as oxygen transport membranes, *J. Eur. Ceram. Soc.* 44 (15) (2024) 116742.